Supplementary Information (SI) for Physical Chemistry Chemical Physics.
This journal is © the Owner Societies 2026

Supporting Information

Indole-Capped Gold Nanoprisms as Multifunctional Nano-platforms: DNA Binding, Mercury Sensing, and Biological Activities

Amar Ghosh,[a,*] Murugesan Panneerselvam,[b] Himal Das,[a] Sourav Mondal,[c] Abhishek Mohanta,[d] Samaresh Paria,[e] Uday Kumar Ghorui,[f] Prasanta Das,[g] Madhuchhanda Das,[h] Rapti Goswami,[a] Susmita Chowdhury,[a] Frederico W. Tavares,[b,i] Dulal Senapati,[c] Amalesh Samanta,[d] Maidul Hossain,[e] Sabyasachi Chakrabortty,[f,j] Arunima Sengupta,[h] Ujjal Kumar Sur,[k,*] Suman Das[a,*]

[a]*Biophysical Chemistry Laboratory, Physical Chemistry Section, Department of Chemistry, Jadavpur University, Raja S. C. Mullick Road, Jadavpur, Kolkata 700 032, India*

[b]*Chemical Engineering Program (PEQ/COPPE), Federal University of Rio de Janeiro (UFRJ), CEP:21941-594, RJ, Brazil*

[c]*Chemical Sciences Division, Saha Institute of Nuclear Physics, A CI of Homi Bhabha National Institute,1/AF, Bidhannagar, Kolkata-700064, India*

[d]*Division of Microbiology & Pharmaceutical Biotechnology, Department of Pharmaceutical Technology, Jadavpur University,188 Raja S.C. Mullick Road, Jadavpur, Kolkata 700032, India.*

[e]*Department of Chemistry, Vidyasagar University, Midnapore, 721102, West Bengal, India*

[f]*Department of Chemistry, School of Engineering and Sciences (SEAS), SRM University AP, Amaravati 522240, Andhra Pradesh, India*

[g]*Department of Chemistry, Faculty of Sciences, Ganpat University, Ganpat Vidyanagar, Kherva, Dist. Mehsana, P.O. 384012, Gujarat, India*

[h]*Department of Life Science and Biotechnology, Jadavpur University,188 Raja S.C. Mullick Road, Jadavpur, Kolkata 700032, India*

[i]*Chemical and Biochemical Process Engineering, School of Chemistry, Federal University of Rio de Janeiro (UFRJ), CEP:21941-594, RJ, Brazil*

[j]*Centre for Interdisciplinary Research, SRM University AP, Amaravati 522240, Andhra Pradesh, India*

[k]*Department of Chemistry, Behala College, Kolkata-700060, India*

Corresponding Author: Suman Das (sumandas10@yahoo.com)

1. Experimental section

1.1. Experimental Solutions

CT-DNA was dissolved in 10 mM Citrate-Phosphate buffer (CP buffer) of pH 7.0, and an identical size around 200 base pairs in average length was prepared by sonication. For the spectroscopic studies, the concentration of CT-DNA was determined using a molar extinction coefficient value of 13,200 M^{-1} cm^{-1} at λ_{max} of 260 nm (expressed in terms of molarity of base pairs).[1-3] The nativeness of the CT-DNA was recorded by monitoring the thermal melting studies at 260 nm. DAPI and EtBr were dissolved in aqueous medium, and their concentration was calculated spectrophotometrically using a molar extinction coefficient of 27,000 M^{-1} cm^{-1} (λ_{max} at 340 nm) and 5680 M^{-1} cm^{-1} (λ_{max} at 480 nm), respectively.[4,5] All the experiments were carried out using an aqueous buffer of 10 mM Na-salt of pH 7.

1.2. Theoretical Investigations: Molecular Docking Simulation

All quantum chemical calculations were carried out using the Gaussian 09 software package.[6] Geometry optimizations and frequency analyses were performed using the unrestricted B3LYP[7,8] (UB3LYP) hybrid functional. For gold (Au) atoms, the LANL2DZ[9] effective core potential (ECP) and associated basis set were employed to account for relativistic effects. For all other non-metal atoms, the 6-311G(d,p)[10,11] basis set was used to ensure a reliable description of valence electron distribution. Frequency calculations were performed at the same level of theory to confirm the nature of the stationary points as true minima (no imaginary frequencies). NCI analysis was performed using the Multiwfn 3.7 program[12] to identify and characterize weak non-covalent interactions in the studied systems. This approach is based on the analysis of the Reduced Density Gradient (RDG), a real-space function derived from the electron density and its derivatives, which is sensitive to non-covalent interactions, such as hydrogen bonding, van der Waals forces, and steric repulsion.

Furthermore, Molecular docking studies were performed to evaluate the binding interactions between CT-DNA[13] and a series of ligands, including Au_1 and Au_8, Trp (Trp), Au_1–Trp, and Au_8–Trp complexes. The Au_8–Trp complexes included various conformers of Trp, including Au_8–Trp4, where Trp was treated as a radical species. All docking calculations were carried out using AutoDock 4.2.[14] The DNA receptor structure was prepared by removing water molecules and adding hydrogen atoms using AutoDockTools (ADT).[14] Ligand structures were optimized using DFT calculations prior to docking and converted to PDBQT format using

ADT. A grid box was centered appropriately to cover the major grooves and minor grooves of CT-DNA, ensuring complete flexibility of the ligand during docking. For each ligand, ten independent docking runs were conducted using the Lamarckian Genetic Algorithm (LGA) with default parameters. The top-ranked docking poses were analyzed based on binding energy (kcal/mol), cluster RMSD, and reference RMSD values. These results were extracted using Grep pattern matching from the AutoDock output log files to identify key docking metrics efficiently. The docking results were visualized using BIOVIA Discovery Studio Visualizer,[15] highlighting key interactions such as hydrogen bonding, π–π stacking, hydrophobic contacts, and charge distribution with CT-DNA. The docking poses with the most favorable binding energies were selected for further interaction analysis and discussion.

1.3. Detection of Hg^{2+} ions by using L-Trp@GNPrs

The detection of mercury ions (Hg^{2+}) using fluorescent gold nanoparticles (AuNPs) involves a sensitive and selective fluorescence and SERS mechanism. Typically, L-Trp-capped AuNPs were synthesized and functionalized with specific ligands such as peptides (L-Trp) that exhibit strong affinity towards Hg^{2+}. Upon the addition of mercury ions into the colloidal solution, the interaction between Hg^{2+} and the ligands on the AuNP surface induces structural changes or facilitates metallophilic interactions (e.g., Au–Hg amalgamation), leading to a significant quenching or shift in the fluorescence emission peak of AuNPs.[16-18] This fluorescence change can be monitored using a spectrofluorometer, allowing for quantitative detection of Hg^{2+} concentrations even at nanomolar levels. In contrast, the enhancement of Raman intensity of L-Trp@GNPrs in the presence of Hg^{2+} ions was further utilized to quantify the limit of detection (LOD) for mercury sensing. The sensing process is typically rapid, label-free, and highly selective due to the unique coordination property of Hg^{2+}, enabling its detection in complex biological or environmental samples.

1.4. MTT Assay: *In Vitro* Cell Viability

MTT (3-[4,5-Dimethylthiazol-2-yl]-2,5-diphenyl tetrazolium bromide) assay was carried out to monitor cell viability upon treatment of L-Trp@GNPrs for different time points.[19] H9c2 Cardiomyocyte cells were cultured in 96-well plates and treated with different concentrations of L-Trp@GNPrs (0, 10, 25, 50, 75, and 100 μg/ml). After that, the cells were incubated for 24, 48, and 72 h at 37°C with 5% atmospheric CO_2. A control experiment was also performed using L-tryptophan and gold salt as a positive control. When the MTT solution had formed a crystal violet tint, it was discarded and replaced with an extraction buffer after 3–4 hours. The resulting formazan crystal color's absorbance was measured at 570 nm with a spectrophotometer. Finally, the cell viability percentage and proliferation percentage were compared with those of untreated cells. We recorded the data in triplicate and quantified the cytotoxicity as a percentage of cell viability, and used the standard error of mean to show the error bar.

1.5. Antioxidant Assay

The antioxidant potential of L-Trp@GNPrs was evaluated using the DPPH (2,2-diphenyl-1-picrylhydrazyl) free radical scavenging assay.[20-22] DPPH, a stable free radical characterized by a deep violet color, which undergoes a visible color change to yellow or becomes colorless upon reduction by an antioxidant. In this study, a 0.1 mM DPPH solution was prepared in ethanol, and L-Trp@GNPrs nanoparticles were added to the solution, which was then incubated for 8 h under dark conditions to prevent photodegradation. After the incubation period, aliquots of the sample at varying concentrations (25, 50, 75, and 100 µg/mL) were collected, and their absorbance was measured at 517 nm using a UV-Vis spectrophotometer [Shimadzu EcoCell (UV-1900i)]. The scavenging activity of the nanoparticles was quantified using the following equation:

$$Scavenging\ Activity\ (\%) = \left(\frac{A_0 - A_S}{A_0}\right) \times 100 \qquad (1)$$

Where A_0 is the absorbance of the control (DPPH solution without sample) and A_s is the absorbance of the test sample containing nanoparticles. This assay helps in quantifying the antioxidant efficiency of the L-Trp@GNPrs based on their ability to neutralize free radicals.

1.6. Antimicrobial Activity

Antibacterial potency of the tryptophan as control group and synthesized L-Trp@GNPrs containing tryptophan on the gold surface was observed by the well diffusion technique with some modifications.[23] Antibacterial potency of the both samples were measured in 3 different concentrations (50, 100, and 200 µg/ml) against both Gram positive *Staphylococcus aureus* ATCC 29737 and Gram-negative *Escherichia coli* MTCC 40 organisms. A control experiment was also performed using L-trptophan. Colonies of bacterial strains cultured in a nutrient broth media were prepared separately. Bacterial suspension (0.1 ml) spread over the nutrient agar plate and allowed to bacterial growth into the incubator. With the help of a borer wells were made on the solidifying plate and required amount of the preparation and control group were poured into the well and incubated for 48 h at 37 °C. The zone of inhibition was observed and measured with the help of a metric ruler and the result was noted.

2. Characterization technique of L-Trp@GNPrs

2.1. UV-visible-NIR absorption spectroscopy

The size, shape, and composition of the plasmonic nature of bare L-Trp@GNPrs can be monitored by studying absorption spectra using a JASCO-V770 UV-Vis-NIR spectrometer within the wavelength range of 1400 to 200 nm with a cell of 1 cm path length. We have diluted the centrifuged sample (3 µL to 1 mL) in Milli-Q ultrapure water (resistivity of 18.2 MΩ.cm at 298.15 K) to measure absorbance.

2.2. Fourier transform infrared spectroscopy (FTIR)

IR spectra of L-Trp solution and L-Trp@GNPrs were measured using an FT-IR spectrophotometer (Alpha II, Bruker Optics) coupled with the attenuated total reflectance (ATR). Spectra were acquired in the range of 4000 - 500 cm^{-1} with 2 cm^{-1} spectral resolution and an average over 128 scans. For measuring IR spectra about 50 µL solution was placed and protected with a convex cover slip. The solvent water and/or water-methanol mixture was used for background spectra.

2.3. X-ray diffraction (XRD) measurements

XRD measurement was carried out in a Rigaku XRD diffractometer within a 2θ range of 20° to 90° operating at Cu-K(α)-Ni filter radiation of 1.5418 Å wavelength, 40 kV voltage, and 30 mA current with a scanning speed of about 0.005°/sec. Before each measurement, the centrifuged samples were deposited as a uniform coating on a glass slide and dried overnight. The strong adhesion property of the samples with the glass slides helped us not to use any binder during the sample deposition.

2.4. Hydrodynamic size and surface charge of nanoparticles

Dynamic Light Scattering (DLS) studies to get an idea about the hydrodynamic diameter and zeta potentials to understand the surface charge of these nanomaterials were performed using a Malvern-made Zetasizer ZS90 instrument. Before every measurement, the dilution of each sample was carried out in the same ratio as previously stated in the case of UV-vis-NIR measurements.

2.5. Scanning electron microscopy (SEM) and Energy-dispersive X-ray spectroscopy (EDX)

A Zeiss Supra 40, Field Emission SEM instrument was used for all SEM analysis. Samples for SEM measurement were prepared on a p-type silicon wafer by injecting 20 µL of (1:1) diluted sample onto it and drying it overnight under ambient conditions. The compositional analysis was done by energy-dispersive X-ray spectroscopy (EDX) attached to Zeiss Supra 40.

2.6. Transmission electron microscopy (TEM), High-resolution Transmission electron microscopy (HRTEM), selected area diffraction pattern (SEAD), and Energy-dispersive X-ray spectroscopy (EDX)

TEM and HRTEM were measured by a JEOL (Japan) JEM-2100 microscope operating at 200 kV. The compositional analysis was done by energy-dispersive X-ray spectroscopy (EDX) attached to JEOL (Japan) JEM-2100. We used a dip and dry method for preparing TEM grids. In briefs, a carbon-coated Cu-grid was dipped into the concentrated sample to allow a monolayer coating onto it, after which it was dried overnight under ambient conditions. The selected area diffraction pattern (SEAD), morphology, and d spacing were obtained through the same microscope at a voltage of 200 kV.

2.7. X-ray Photoelectron spectroscopy (XPS) measurements

The oxidation state and binding energy of the materials were identified with an X-ray photoelectron spectroscopy (XPS) PHI Versaprobe III using a mono-energetic Al Kα source with an energy of 1486.6 eV to analyse the sample surface. All the samples were prepared on silicon wafers by a drop-casting method.

2.8. Inductively Coupled Plasma Optical Emission Spectrometry (ICP-OES)

The elemental concentration of L-Trp@GNPrs was determined by inductively coupled plasma optical emission spectrometry (ICP-OES) on a Thermo Scientific iCAP 7000 spectrometer (Perkin Elmer, Waltham, MA, USA). NIST standards of 50 ppb, 0.5 ppm, 1 ppm, 15 ppm, 25 ppm, 50 ppm, and 100 ppm were used for Au concentration determination. The wavelengths selected for Au were 242.7 nm, 267.5 nm, and 283.5 nm, and for S were 182.0 nm and 182.6 nm respectively. Before each measurement, the centrifuged samples are diluted (50µL to 15mL) in Milli-Q ultrapure water and digested for 1.5 h at 60 °C.

3. DFT Calculation of Synthesized Nanomaterials

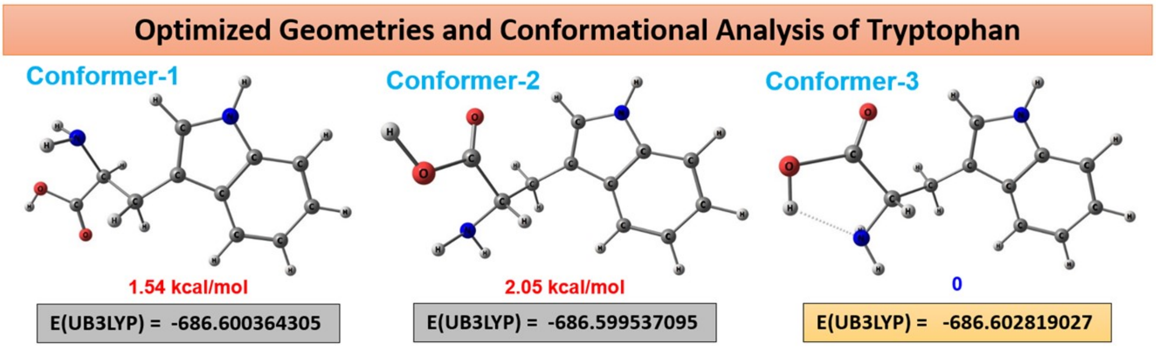

Figure S1. Optimized Geometries and Conformational Analysis of Tryptophan along with their total energies.

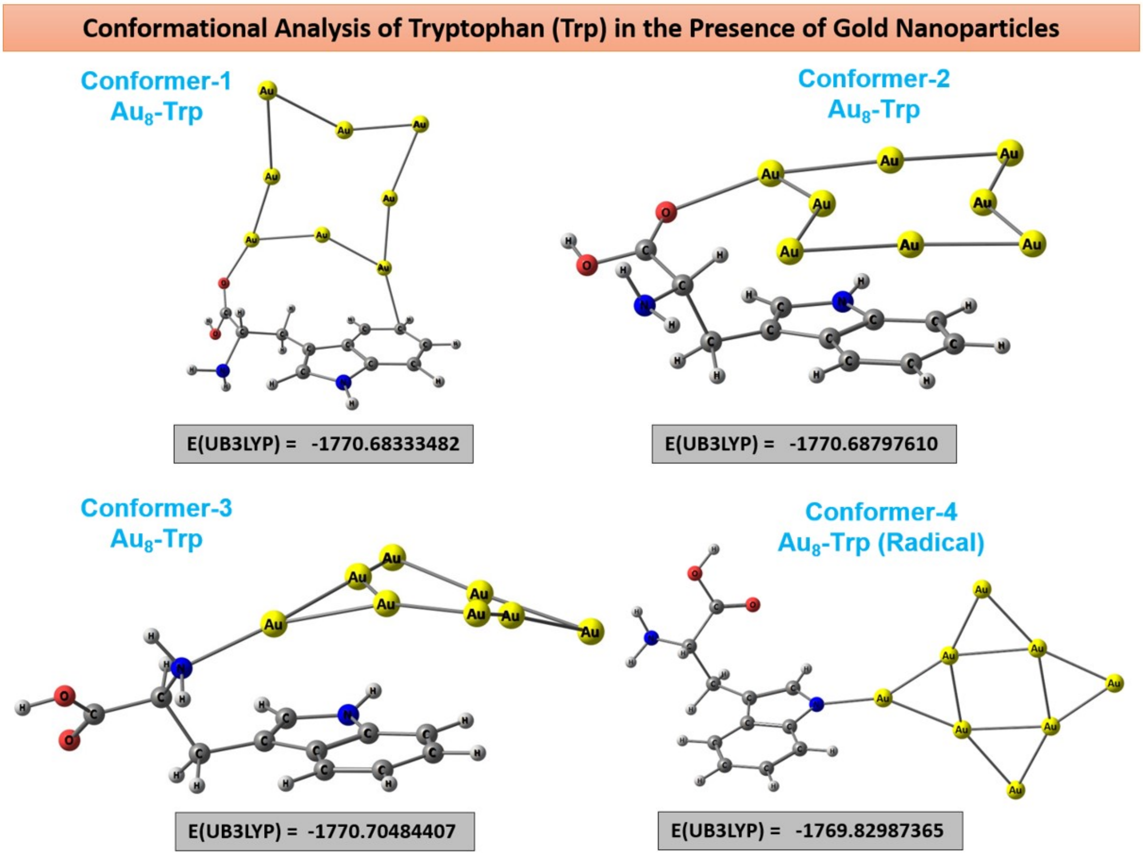

Figure S2. Conformational analysis of tryptophan (Trp) in the Presence of gold nanoparticles along with their total energies.

4. Surface characterization of L-Trp@GNPrs

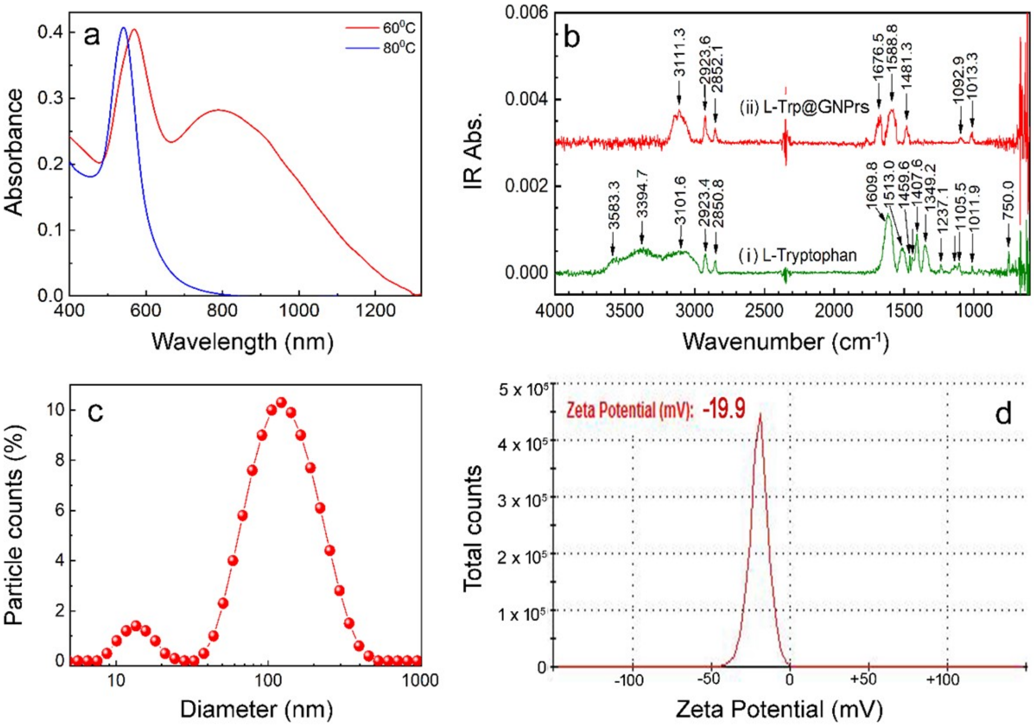

Figure S3. (a) Absorption spectra of synthesized L-trptophan stabilized gold nanoparticles at two temperatures i.e., red line for 60 °C and blue line for 80 °C, respectively. (b) FTIR spectra of L-Tryptophan (i) and L-Trp@GNPrs (ii), respectively. (c) point plot of the particle size distribution of L-Trp@GNPrs with an average hydrodynamic diameter (d_h) around 122 nm. (d) Zeta potential of L-Trp@GNPrs with negative value at -19.9 mV.

Table S1: DLS, PDI, and Zeta potential values of synthesized gold nanoparticles at two different temperatures.[a]

Type of Nanomaterials	DLS (nm)	PDI	Zeta Potential (mV)
$\mathrm{NP}_{60\ °\mathrm{C}}$	122.3 ± 12.5	0.463	-19.9
$\mathrm{NP}_{80\ °\mathrm{C}}$	78.82 ± 8.9	0.221	-4.94

[a] All data in this table are an average of three determinations.

5. Size and shape determined by Field emission-scanning electron microscopy images

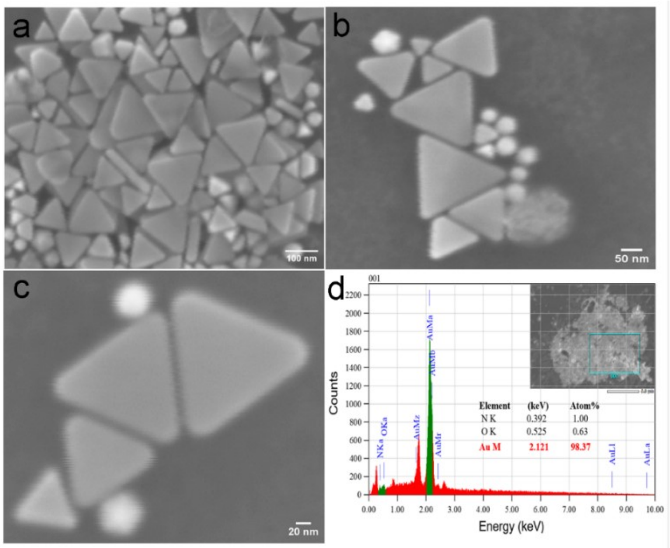

Figure S4. (a), (b) and (c) are the FE-SEM images of L-Trp@GNPrs at different magnifications, and (d) EDAX spectrum of L-Trp@GNPrs obtained from SEM.

6. Size and shape determined by transmission electron microscopy images of $\mathrm{NP}_{80\,^{\circ}\mathrm{C}}$

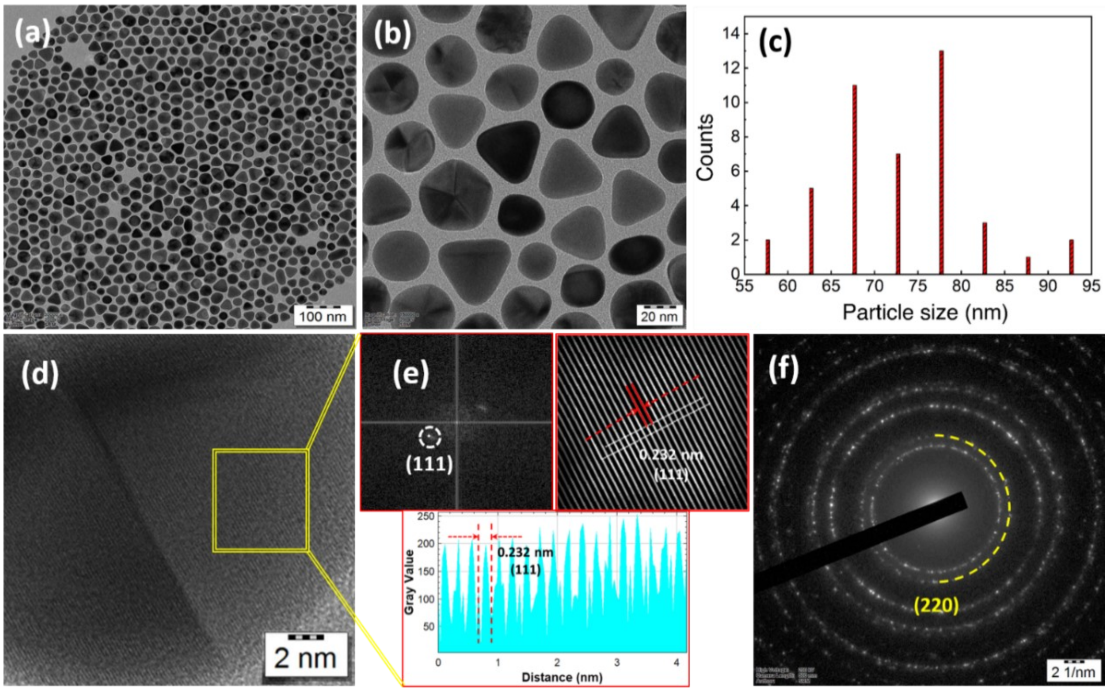

Figure S5. (a) and (b) are the TEM images with different magnification of L-Trp capped gold nanoparticles ($\mathrm{NP}_{80\,^{\circ}\mathrm{C}}$) synthesized at 80 °C temperature, (c) Particle size distribution of $\mathrm{NP}_{80\,^{\circ}\mathrm{C}}$ obtained from TEM analysis, (d) and (e) HRTEM image of $\mathrm{NP}_{80\,^{\circ}\mathrm{C}}$ showing lattice planes with a spacing of 0.232 nm corresponding to (11) Bragg's plane, and (f) SAED pattern showing polycrystalline in nature with containing (220) Bragg's plane of the $\mathrm{NP}_{80\,^{\circ}\mathrm{C}}$.

Figure S5(a,b) displays TEM images of the nanoparticles, synthesized at 80 °C ($NP_{80\,°C}$). These structures are primarily pseudospherical, highly monodisperse, and significantly smaller in size (average diameter < 100 nm) than the edge length of the triangular nanoprisms. Notably, no anisotropic structures were observed at this higher synthesis temperature. Particle size distribution (Figure S5c) shows an average diameter of ~78 nm. The calculated lattice spacing of 0.232 nm from HRTEM analysis, as shown in Figure S5(d,e), corresponds to the (111) lattice planes of face-centered cubic (fcc) gold. Moreover, SAED patterns (Figure S5f) provide clear evidence for the presence of the high-energy {200} facet in $NP_{80\,°C,}$ which is also present in the XRD profile.

7. Photophysical Property of L-Trp@GNPrs

The fluorescence quantum yield (ϕ) is defined as the ratio of the number of photons emitted to the number of photons absorbed;

$$\phi = \frac{Number\ of\ photons\ emitted}{Number\ of\ photons\ absorbed} = \frac{I_f}{I_a} \qquad (1)$$

However, the relative quantum yield is generally determined by comparing the sample to a reference fluorophore with a known quantum yield (coumerin-153, ϕ_R = 53%) using the following relation;[24]

$$\phi_S = \left(\frac{I_S}{I_R}\right)\left(\frac{A_R}{A_S}\right)\left(\frac{\eta_S}{\eta_R}\right)^2 \phi_R \qquad (2)$$

Where the term ‘I’ signifies for the integrated area under the fluorescence curve. ‘A’ and ‘η’ denote the absorbance and refractive index of the medium, respectively (η_S/η_R=1, in aqueous solutions). The subscripts ‘S’ and ‘R’ used in each term in the above equation stand in recognition of sample and reference, respectively. Therefore, it can be modified as,

$$\phi_S = \left(\frac{k_S}{k_R}\right)\phi_R \qquad (3)$$

Here ‘k’ is the slope of the integral area under fluorescence spectra (λ_{ex}=280 nm) to absorbance. By plotting fluorescence intensity versus absobance of the L-Trp@GNPrs and coumerin-153 as a sample and reference respectively, we evaluated quantitatively the fluorescence quantum yield of synthesized L-Trp@GNPrs and was found to be 62.3 %. Lastly, in basic pH, the intensity of fluorescence emission was increased (Figure S6e) because of acidic groups in the vicinity of Trp (like –COOH) can lose protons (H^+), leading to conformational changes in proteins, causes partial unfolding or exposure of Trp to polar solvent (like water). At low pH, the damping of fluorescence intensity was observed (Figure S6e), which suggested that amino groups ($-NH_2$) are protonated to $-NH_3^+$ and carboxyl groups ($-COO^-$) become neutral -COOH. These changes modify the electrostatic environment around Trp, which can affect its fluorescence property. However, the fluorescence intensity of L-Trp@GNPrs changes with the influence of pH, which confirms that the abundant –COOH and –NH2 groups were present on the surface of L-Trp@GNPrs.

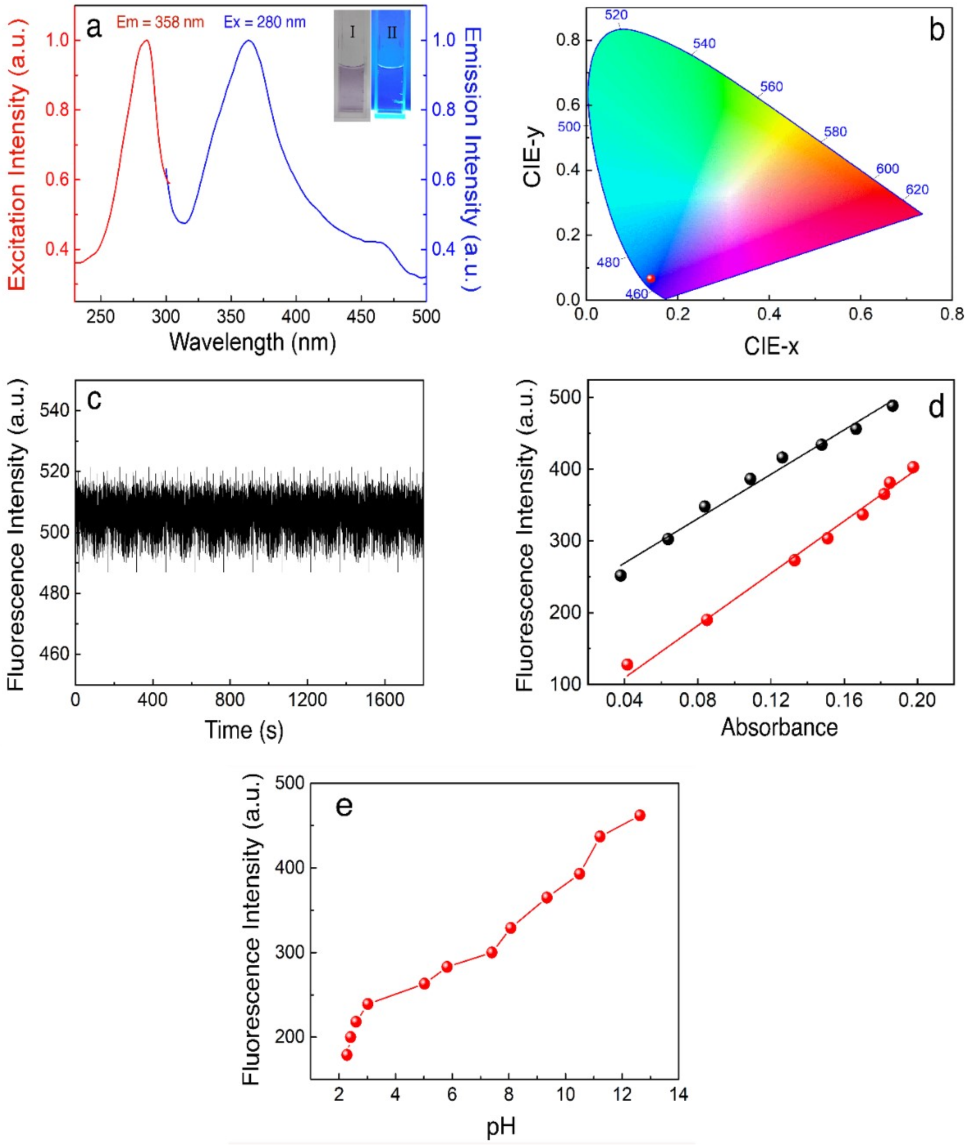

Figure S6. (a) Steady-state fluorescence excitation (red line) and emission (blue) spectra of L-Trp@GNPrs; Inset of (a) shows the color of L-Trp@GNPrs dispersion in absence and presence of UV-lamp at 280 nm, (b) CIE 1931 color space coordinate, (c) Fluorescence spectra of L-Trp@GNPrs towards the irradiation time, (d) Plots of fluorescence intensity against absorbance of coumerin-153 (black line) and L-Trp@GNPrs (red line), respectively, and (e) Fluorescence spectra of L-Trp@GNPrstowards the influences of different pH.

8. Characterization of L-Trp@GNPrs-CT DNA complexation

Steady state absorption spectral titration was carried out in Shimadzu spectrophotometer (model UV-1900, Shimadzu Corporation, Japan) and JASCO-V770 UV-vis-NIR spectrometer within the wavelength range of 1400 to 400 nm and matched quartz cuvettes with a path length of 1 cm. Steady-state fluorescence spectral studies were performed on Shimadzu RF5301PC spectrofluorimeter (Shimadzu Corporation, Japan) and Horiba Jobin Yvon fluoromax-4 spectrofluorimeter with an attached thermo programmer controlled by the Peltier effect. The entire investigation of the intrinsic fluorescence of L-Trp@GNPrs was carried out in a fluorescence-free quartz cell with a 1 cm path length and an excitation and emission slit of 5 and 15 nm respectively. Time-correlated single photon counting (TCSPC) experiments were employed on a Hamamatsu MCP photomultiplier (R3809) and analyzed using IBH DAS6 software. The excitation wavelength of 280 nm was done using a nanosecond diode laser (IBH NanoLED 07) in an IBH fluorocube setup. Circular dichroism (CD) spectra were recorded on a PC-driven JASCO J815 spectropolarimeter (Jasco International Co., Japan) equipped with a thermal programmer (model PFD-425L/15) and temperature controller interfaced in a rectangular quartz cuvette of 1 cm path length. All the CD spectra were recorded with a scan speed of 100 nm/min within the 195−300 nm wavelength range. Atomic Force Microscopy (AFM) experiments were performed on through well-equipped Agilent 5500 AFM (USA) instrument using tapping mode with 100 μm cantilever length. Gwyddion 2.62 was used for visualization and analysis of the images. Electron imaging was recorded by a JEOL-made TEM-2100 Plus Electron microscope operating at 200 kV. The compositional analysis was done by energy-dispersive X-ray spectroscopy (EDX) attached to TEM-2100 Plus Electron microscope. Isothermal titration calorimetry (ITC) experiments in this study were conducted using a Nano ITC instrument (TA Instruments, Waters, New Castle, USA) at three different temperatures: 298.15 K, 303.15 K, and 308.15 K. Firstly, air bubbles are eliminated and for all the experimental solutions were degassed on supplied degas station. After degassing, 1.5 mL of a 0.1 mM nanoparticle dispersion was loaded into the calorimeter cell. A 250 μL syringe, rotating at 290 rpm, was used to inject 10 μL aliquots of degassed CT-DNA (1.0 mM) into the nanoparticle dispersion. To account for the heat of dilution, control titrations were carried out by injecting the same DNA solution into blank buffer under identical conditions. The heat of dilution was subtracted from the total heat change measured during L-Trp@GNPrs–DNA complexation. Data analysis was performed using NanoAnalyze software provided by the manufacturer. From the corrected heat vs. mole ratio plots, the enthalpy change (ΔH°) and equilibrium binding constant (Ka) were determined. The Gibbs free energy change (ΔG°) and entropy term ($T\Delta S^\circ$) were then calculated using the standard thermodynamic relationships: $\Delta G^\circ = - RT \ln K_a = \Delta H^\circ - T\Delta S^\circ$, where T is the temperature in kelvin and R is the universal gas constant.

9. UV-Visible Absorption Spectral Study of L-Trp@GNPrs-DNA complexation

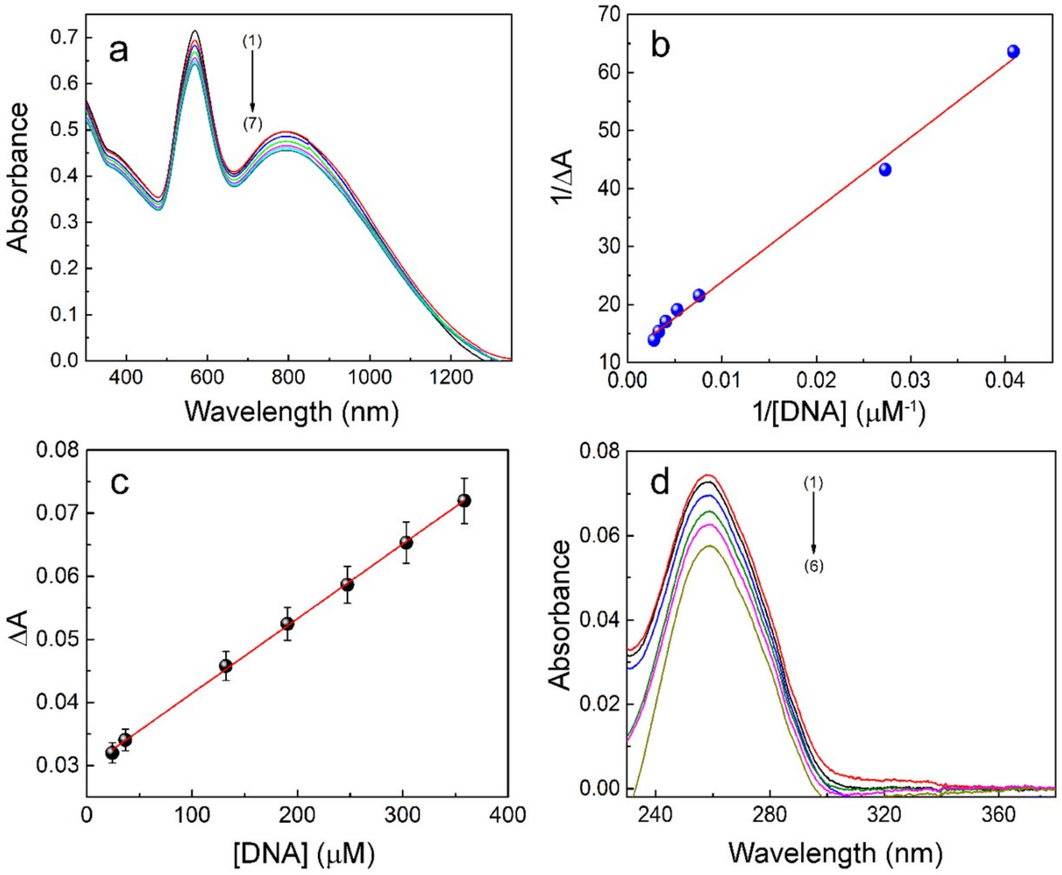

Figure S7. UV-Visible absorption spectra of L-Trp@GNPrs (a) in absence and presence of different concentrations of CT-DNA; (a) curves (1-7) represent the spectral changes of L-Trp@GNPrs (92.28 μM) treated with 0.0, 12.25, 24.46, 36.62, 190.38, 303.49, and 358.45 μM CT-DNA, (b) Benesi-Hildebrand plot of 1/ΔA vs 1/[DNA] for binding interaction, (c) plots of ΔA vs [DNA] for determination of LOD of DNA, and (d) absorption spectra of CT-DNA in absence and presence of L-Trp@GNPrs; (d) curves (1-6) represent the spectral changes of CT-DNA (5.31 μM) treated with 0.0, 11.51, 23.03, 34.51, 46.0, and 57.47 μM L-Trp@GNPrs.

10. Fluorescence Spectral titration of L-Trp solutions against CT-DNA

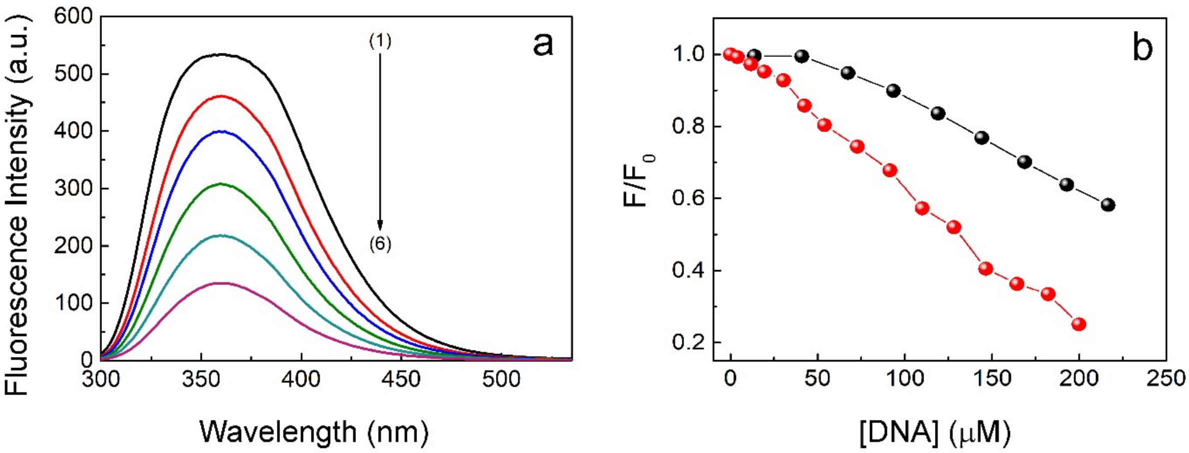

Figure S8. (a) Fluorescence spectra of L-Trp in the absence and presence of CT-DNA; curves (1-6) of (a) represent the spectral changes of L-Trp (46.14 μM) on addition of 0, 31, 72, 109, 146, and 200 μM of CT-DNA, (b) F/F$_0$ vs [DNA] plot of L-Trp@GNPrs-DNA (black ball) and L-Trp-DNA (red ball) systems, respectively.

11. Evaluation of Stern-Volmer quenching at three temperatures by spectrofluorometry

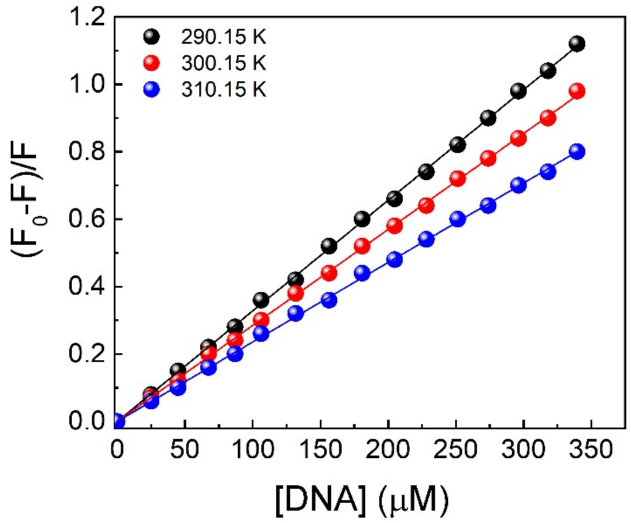

Figure S9. Stern-Volmer quenching plots of L-Trp@GNPrs at 290.15, 300.15, and 310.15 K in an aqueous buffer of 10 mM Na-salt of pH 7.

Table S2. Temperature-dependent fluorescence quenching constants (K_{SV}) and bimolecular quenching constants (k_q) of L-Trp@GNPrs-DNA system in an aqueous buffer of 10 mM Na-salt of pH 7.

System	Temperature (K)	$K_{SV} \times 10^{-3}$ (M^{-1})	$k_q \times 10^{-13}$ ($M^{-1}\ s^{-1}$)
L-Trp@GNPrs-DNA	290.15	3.28 ± 0.37	5.50 ± 0.37
	300.15	2.85 ± 0.18	4.40 ± 0.18
	310.15	2.36 ± 0.27	3.63 ± 0.27

12. Kinetic study of L-Trp@GNPrs-DNA system at three different temperatures

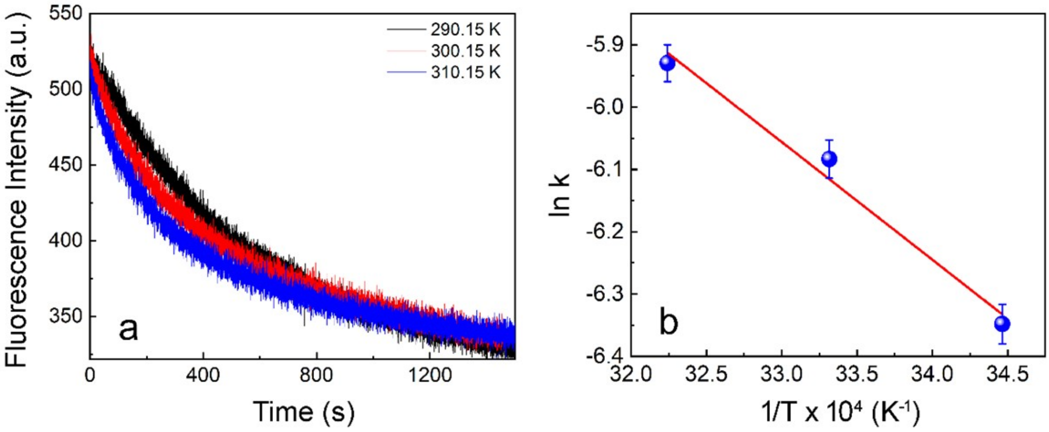

Figure S10. (a) Fluorescence quenching plots of L-Trp@GNPrs in presence of CT-DNA with times at 290.15, 300.15, and 310.15 K and (b) variation of the natural logarithm of rate constant (k) as a function of 1/T at three respective temperatures in an aqueous buffer of 10 mM Na-salt of pH 7, respectively.

Table S3. Time-resolved fluorescence decay data of L-Trp@GNPrs (23.07 mM) in absence and presence of DNA in aqueous buffer at 298.15 K.

System	[DNA]/[GNPrs]	τ_1 (ns)	A_1	τ_2 (ns)	A_2	τ_3 (ns)	A_3	$<\tau>$ (ns)	χ^2
L-Trp@GNPrs	0.0	0.19	0.875	2.84	0.60	-	-	0.649	1.13
	0.76	2.12	0.163	4.18	0.05	0.159	0.78	0.685	1.00
	3.02	1.96	0.155	4.40	0.05	0.178	0.78	0.692	1.04
	4.13	2.01	0.138	4.67	0.04	0.160	0.81	0.618	1.10
	5.23	2.08	0.136	5.10	0.03	1.61	0.82	0.613	1.01

13. Dye Displacement and Evaluation of the modified Stern-Volmer quenching constant of the DAPI-DNA system by spectrofluorometric titration

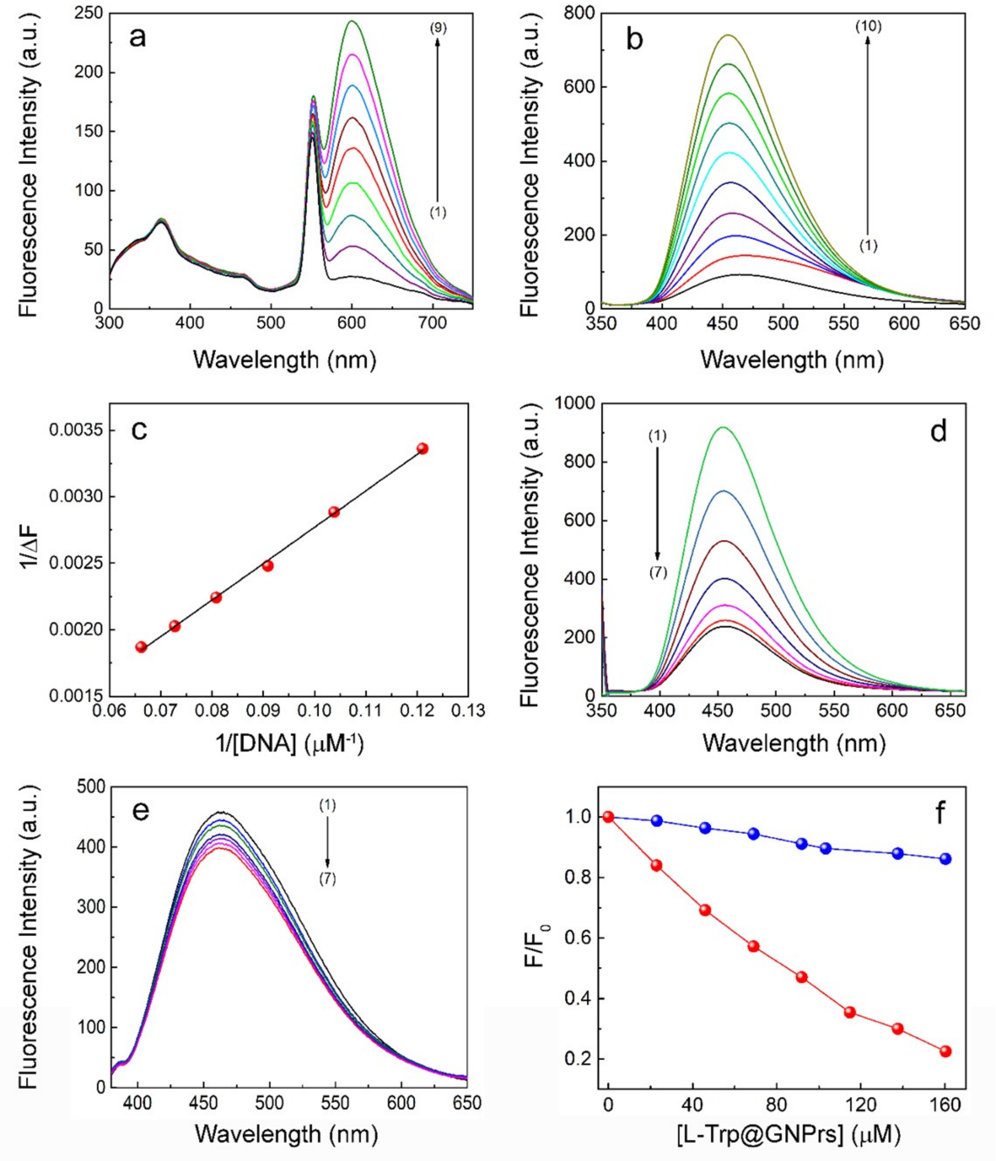

Figure S11. (a) Displacement assay of L-Trp@GNPrs-DNA with gradual addition of EtBr; curves (1-9) of (a) represent the spectral changes of L-Trp@GNPrs-DNA complex on addition of 0.0, 0.2, 0.4, 0.6, 0.8, 1.0, 1.2, 1.4 and 1.6 μM of EtBr, (b) Enhancement of Fluorescence intensity of DAPI in presence of DNA; curves (1-10) of (b) represent the spectral changes of DAPI (3.23 μM) on addition of 0.0, 2.75, 4.13, 5.51, 6.88, 8.26, 9.65, 11.00, 12.37 and 13.74 μM of CT-DNA, (c) Displacement assay of DAPI-DNA system with gradual addition of L-Trp@GNPrs; curves (1-7) of (c) represent the spectral changes of DAPI-DNA complexation on addition of 0.0, 46.04, 69.00, 91.91, 114.77, 137.59 and 160.36 μM of L-Trp@GNPrs, (d) Modified Stern-Volmer quenching plot of 1/ΔF verses 1/[DNA] in the DAPI-DNA system, (e) Fluorescence spectra of DAPI in the absence and presence of L-Trp@GNPrs; curves (1-7) of (e) represent the spectral changes of DAPI (3.23 μM) on addition of 0, 23, 46, 68, 91, 114 and 160 μM of L-Trp@GNPrs and (f) F/F_0

vs [L-Trp@GNPrs] plots of fluorescence titration of free DAPI (blue ball) and DNA-bound DAPI in presence of L-Trp@GNPrs (red ball), respectively.

14. Viscosity measurement of CT-DNA in presence of L-Trp@GNPrs

Viscosity measurement is a classical and effective technique for investigating the conformational changes and binding interactions of DNA with small molecules, proteins, or nanomaterials. This method is particularly valuable in differentiating various DNA binding modes, such as intercalation, groove binding, and electrostatic interactions. In this study, viscosity experiments were conducted using a Cannon-Manning semi-micro dilution Ostwald viscometer (type 75; Cannon Instruments Co., State College, PA, USA), which was vertically immersed in a thermostatically controlled water bath maintained at (20 ± 1) °C.[25] A volume of 600 μL of calf thymus DNA (CT-DNA) solution (800 μM) was introduced into the viscometer, and defined aliquots of L-Trp@GNPrs nanoparticle stock solutions were subsequently added using a microsyringe to achieve a [L-Trp@GNPrs]/[DNA] molar ratio ranging from 0.1 to 0.8. The corresponding nanoparticle concentration varied from 57 μM to 451 μM. Viscosity was determined by averaging the flow times from ten independent measurements at a constant temperature of 298.15 K. The relative specific viscosity (η/η_0) of the DNA-nanoparticle system, where η and η_0 represent the viscosity of DNA in the presence and absence of nanoparticles, respectively, was calculated using standard hydrodynamic equations:[26]

$$\frac{\eta}{\eta_0} = \frac{[t_{complex} - t_0]}{[t_{control} - t_0]} \tag{4}$$

Here, η and η_0 are the specific viscosity of DNA in the presence and in absence of L-Trp@GNPrs; $t_{complex}$ and $t_{control}$ are the time of flow of complex and control solution and t_0 is the same for buffer solution as described previously. The viscosity data were further analyzed by expressing the length enhancement per DNA base pair relative to a standard value ($\beta = 1$). The ratio of contour lengths (L/L_o) was derived from the change in relative viscosity[27] using the relation:

$$\frac{L}{L_0} = \left(\frac{\eta}{\eta_0}\right)^{1/3} = 1 + \beta r \tag{5}$$

Where L and L_0 are the contour lengths of DNA inpresence and absence of the synthesized L-Trp@GNPrs, β is the ratio between extension elongated per bound ligand and the distance between two consecutive base-pairs (0.34 nm). For typical intercalors, β = 1.[28,29] As illustrated in Figure S12, the incremental addition of L-Trp@GNPrs nanoparticles resulted in only a marginal change in the viscosity of the CT-DNA solution. The obtained results are similar to the behavior reported in Hu. Et al.[30] This minimal effect on DNA viscosity suggests that the nanoparticles do not intercalate between DNA base pairs. Instead, the data strongly support a groove-binding interaction mechanism, where the nanoparticles likely associate with the minor grooves of the DNA helix without significantly altering its overall contour length.

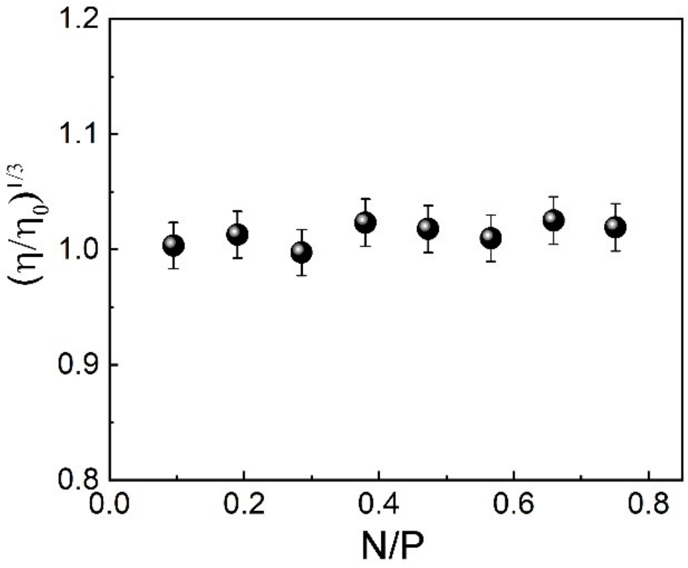

Figure S12. Variation of viscosity with N/P ratio of CT-DNA in presence of L-Trp@GNPrs.

15. Effect of Ionic Strength on Complexation

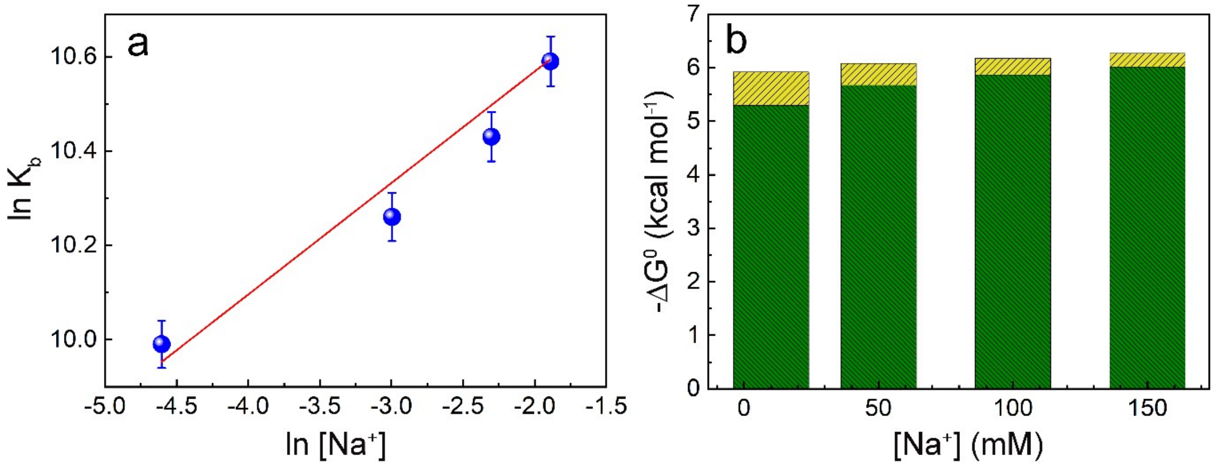

Figure S13. (a) Plot of variation of ln K_b vs ln [Na+] and (b) Partitioned non-polyelectrolytic (olive shed) and polyelectrolytic (yellow hatched) contributions to the standard molar Gibbs free energy change at varying salt concentration.

16. The temperature-dependent standard molar enthalpy changes (ΔH°) were plotted against temperature (T) to determine the standard molar heat capacity change (ΔC_p°)

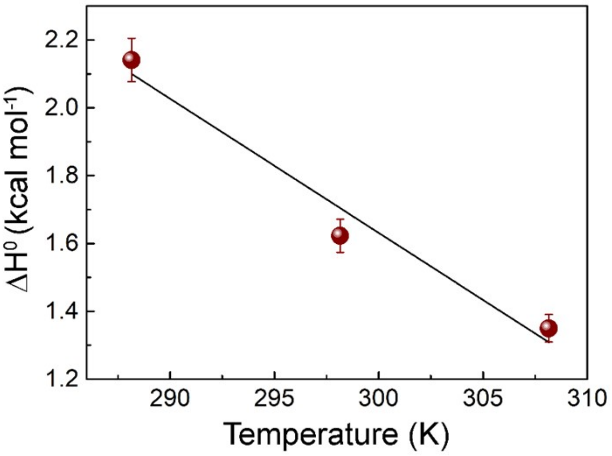

Figure S14. Variation of ΔH° with temperature for the interaction of L-Trp@GNPrs with CT-DNA.

17. AFM image of L-Trp@GNPrs

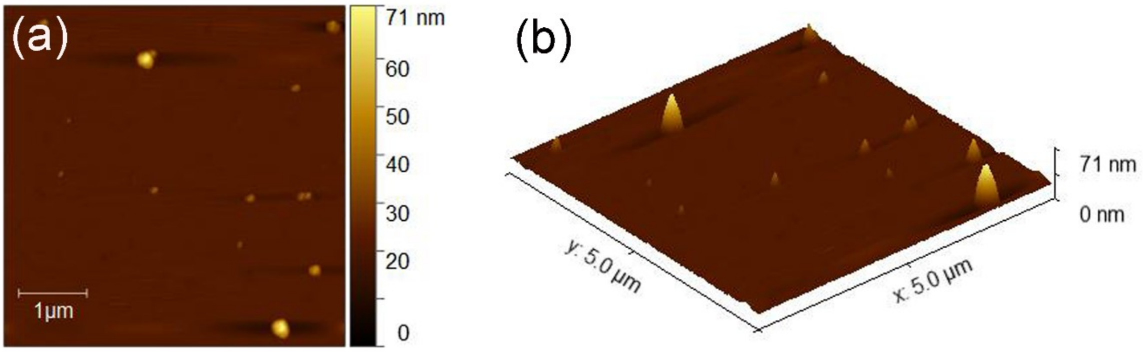

Figure S15. (a) and (b) are the AFM images of air-dried free L-Trp@GNPrs with 2D and 3D topography, respectively.

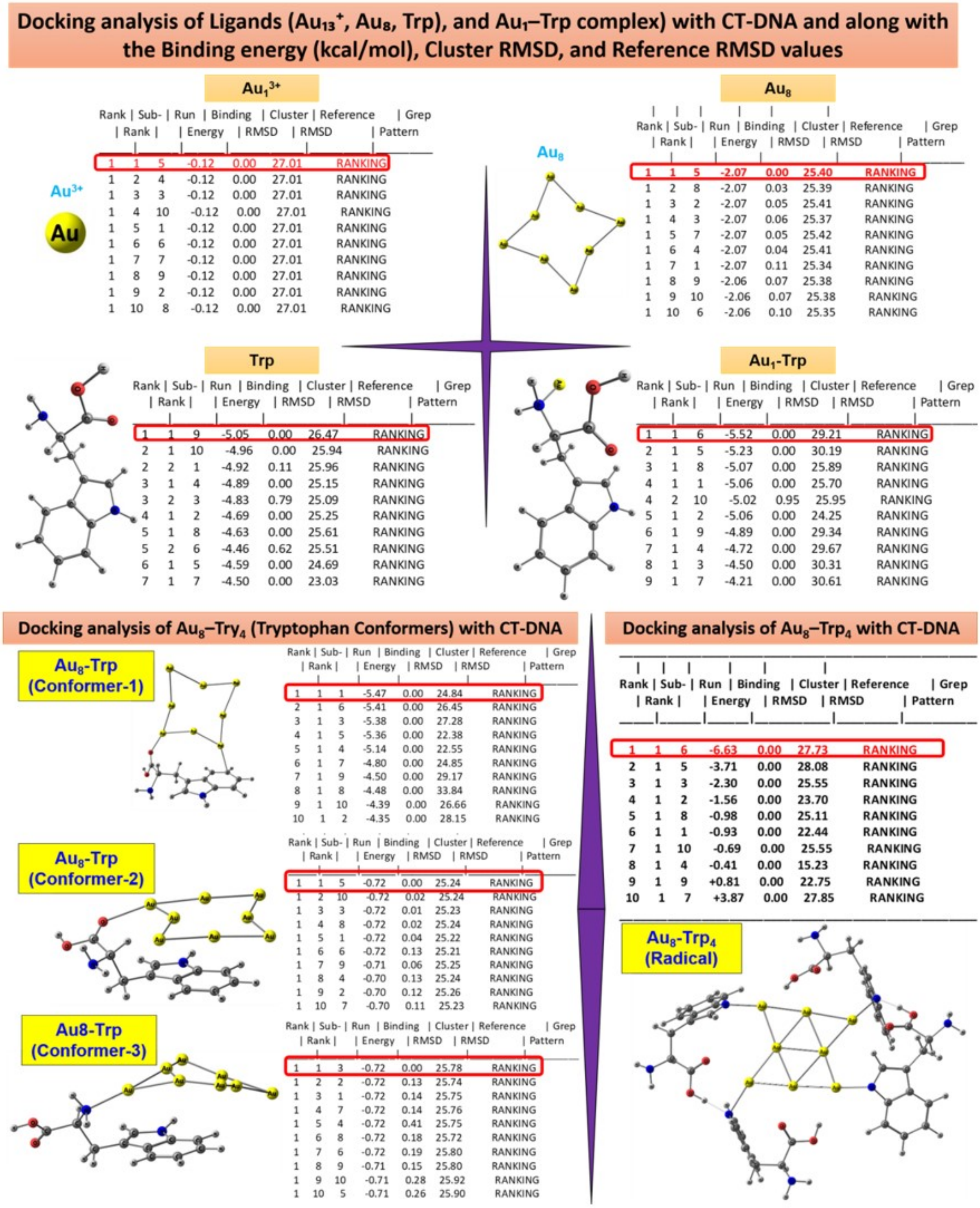

Docking analysis of Ligands (Au_{13}^+, Au_8, Trp), and Au_1–Trp complex) with CT-DNA and along with the Binding energy (kcal/mol), Cluster RMSD, and Reference RMSD values

Au_1^{3+}

```
Rank | Sub- | Run  | Binding   | Cluster | Reference      | Grep
     | Rank |      | Energy    | RMSD    | RMSD           | Pattern
  1     1     5     -0.12     0.00     27.01          RANKING
  1     2     4     -0.12     0.00     27.01          RANKING
  1     3     3     -0.12     0.00     27.01          RANKING
  1     4    10      -0.12     0.00     27.01          RANKING
  1     5     1     -0.12     0.00     27.01          RANKING
  1     6     6     -0.12     0.00     27.01          RANKING
  1     7     7     -0.12     0.00     27.01          RANKING
  1     8     9     -0.12     0.00     27.01          RANKING
  1     9     2     -0.12     0.00     27.01          RANKING
  1    10     8      -0.12     0.00     27.01          RANKING
```

Au_8

```
Rank | Sub- | Run  | Binding   | Cluster | Reference      | Grep
     | Rank |      | Energy    | RMSD    | RMSD           | Pattern
  1     1     5     -2.07     0.00     25.40          RANKING
  1     2     8     -2.07     0.03     25.39          RANKING
  1     3     2     -2.07     0.05     25.41          RANKING
  1     4     3     -2.07     0.06     25.37          RANKING
  1     5     7     -2.07     0.05     25.42          RANKING
  1     6     4     -2.07     0.04     25.41          RANKING
  1     7     1     -2.07     0.11     25.34          RANKING
  1     8     9     -2.06     0.07     25.38          RANKING
  1     9    10      -2.06     0.07     25.38          RANKING
  1    10     6      -2.06     0.10     25.35          RANKING
```

Trp

```
Rank | Sub- | Run  | Binding   | Cluster | Reference      | Grep
     | Rank |      | Energy    | RMSD    | RMSD           | Pattern
  1     1     9     -5.05     0.00     26.47          RANKING
  2     1    10      -4.96     0.00     25.94          RANKING
  2     2     1     -4.92     0.11     25.96          RANKING
  3     1     4     -4.89     0.00     25.15          RANKING
  3     2     3     -4.83     0.79     25.09          RANKING
  4     1     2     -4.69     0.00     25.25          RANKING
  5     1     8     -4.63     0.00     25.61          RANKING
  5     2     6     -4.46     0.62     25.51          RANKING
  6     1     5     -4.59     0.00     24.69          RANKING
  7     1     7     -4.50     0.00     23.03          RANKING
```

Au_1-Trp

```
Rank | Sub- | Run  | Binding   | Cluster | Reference      | Grep
     | Rank |      | Energy    | RMSD    | RMSD           | Pattern
  1     1     6     -5.52     0.00     29.21          RANKING
  2     1     5     -5.23     0.00     30.19          RANKING
  3     1     8     -5.07     0.00     25.89          RANKING
  4     1     1     -5.06     0.00     25.70          RANKING
  4     2    10      -5.02     0.95     25.95          RANKING
  5     1     2     -5.06     0.00     24.25          RANKING
  6     1     9     -4.89     0.00     29.34          RANKING
  7     1     4     -4.72     0.00     29.67          RANKING
  8     1     3     -4.50     0.00     30.31          RANKING
  9     1     7     -4.21     0.00     30.61          RANKING
```

Docking analysis of Au_8–Try_4 (Tryptophan Conformers) with CT-DNA

Au_8-Trp (Conformer-1)

```
Rank | Sub- | Run  | Binding   | Cluster | Reference      | Grep
     | Rank |      | Energy    | RMSD    | RMSD           | Pattern
  1     1     1     -5.47     0.00     24.84          RANKING
  2     1     6     -5.41     0.00     26.45          RANKING
  3     1     3     -5.38     0.00     27.28          RANKING
  4     1     5     -5.36     0.00     22.38          RANKING
  5     1     4     -5.14     0.00     22.55          RANKING
  6     1     7     -4.80     0.00     24.85          RANKING
  7     1     9     -4.50     0.00     29.17          RANKING
  8     1     8     -4.48     0.00     33.84          RANKING
  9     1    10      -4.39     0.00     26.66          RANKING
 10     1     2      -4.35     0.00     28.15          RANKING
```

Au_8-Trp (Conformer-2)

```
Rank | Sub- | Run  | Binding   | Cluster | Reference      | Grep
     | Rank |      | Energy    | RMSD    | RMSD           | Pattern
  1     1     5     -0.72     0.00     25.24          RANKING
  1     2    10      -0.72     0.02     25.24          RANKING
  1     3     3     -0.72     0.01     25.23          RANKING
  1     4     8     -0.72     0.02     25.24          RANKING
  1     5     1     -0.72     0.04     25.22          RANKING
  1     6     6     -0.72     0.13     25.21          RANKING
  1     7     9     -0.71     0.06     25.25          RANKING
  1     8     4     -0.70     0.13     25.24          RANKING
  1     9     2     -0.70     0.12     25.26          RANKING
  1    10     7      -0.70     0.11     25.23          RANKING
```

Au8-Trp (Conformer-3)

```
Rank | Sub- | Run  | Binding   | Cluster | Reference      | Grep
     | Rank |      | Energy    | RMSD    | RMSD           | Pattern
  1     1     3     -0.72     0.00     25.78          RANKING
  1     2     2     -0.72     0.13     25.74          RANKING
  1     3     1     -0.72     0.14     25.75          RANKING
  1     4     7     -0.72     0.14     25.76          RANKING
  1     5     4     -0.72     0.41     25.75          RANKING
  1     6     8     -0.72     0.18     25.72          RANKING
  1     7     6     -0.72     0.19     25.80          RANKING
  1     8     9     -0.71     0.15     25.80          RANKING
  1     9    10      -0.71     0.28     25.92          RANKING
  1    10     5      -0.71     0.26     25.90          RANKING
```

Docking analysis of Au_8–Trp_4 with CT-DNA

```
Rank | Sub- | Run  | Binding   | Cluster | Reference      | Grep
     | Rank |      | Energy    | RMSD    | RMSD           | Pattern
_____|______|______|___________|_________|________________|__________
  1     1     6     -6.63     0.00     27.73          RANKING
  2     1     5     -3.71     0.00     28.08          RANKING
  3     1     3     -2.30     0.00     25.55          RANKING
  4     1     2     -1.56     0.00     23.70          RANKING
  5     1     8     -0.98     0.00     25.11          RANKING
  6     1     1     -0.93     0.00     22.44          RANKING
  7     1    10      -0.69     0.00     25.55          RANKING
  8     1     4     -0.41     0.00     15.23          RANKING
  9     1     9     +0.81     0.00     22.75          RANKING
 10     1     7      +3.87     0.00     27.85          RANKING
```

Au_8-Trp_4 (Radical)

Figure S16. Docking analysis of ligands—Au_1, Au_8, tryptophan (Trp), Au_1–Trp, and Au_8–Trp complexes (including various tryptophan conformers) and Au_8–Trp_4 with tryptophan as a radical species—with CT-DNA. The figure presents binding energy values (kcal mol^{-1}), cluster RMSD, and reference RMSD derived from the top 10 ranked docking poses, extracted using Grep pattern analysis from AutoDock output.

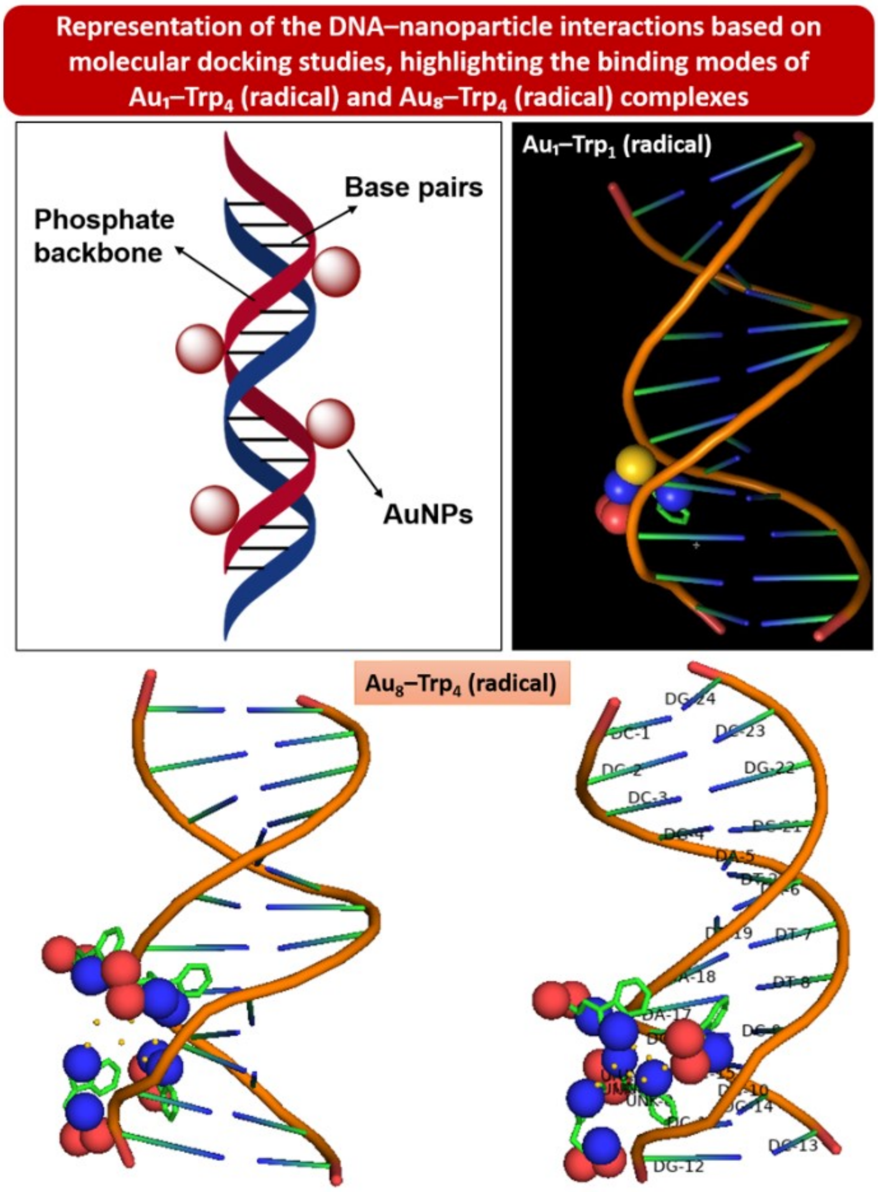

Figure S17. Representation of DNA–nanoparticle interactions from molecular docking studies, illustrating the binding modes of Au_1–Trp_4 (radical) and Au_8–Trp_4 (radical) complexes.

18. Electron Microscopy- imaging of Hg-nanoprism adducts

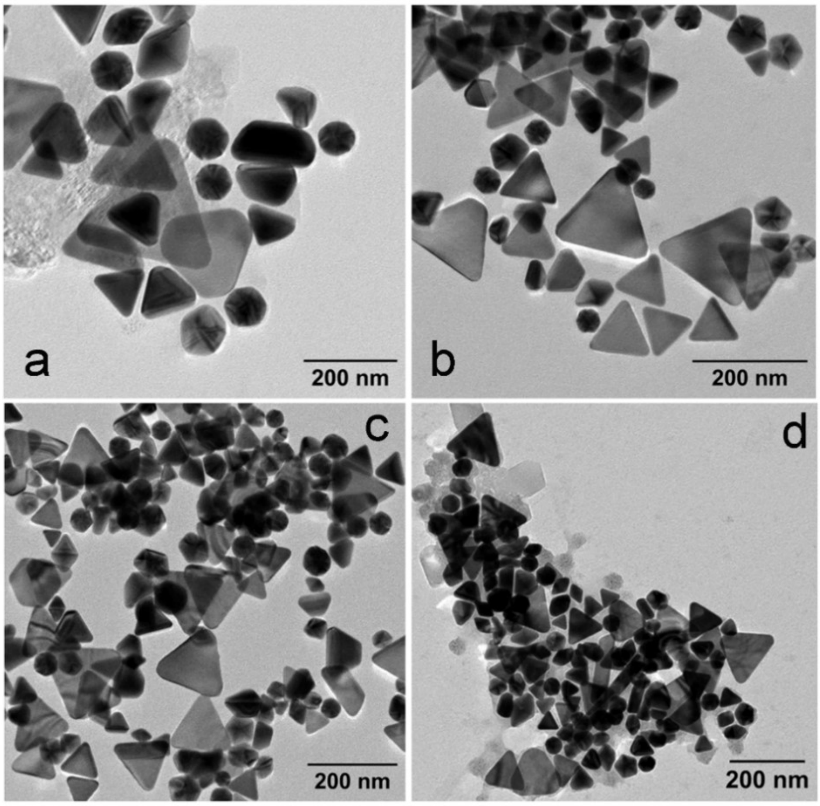

Figure S18. Electron imaging of Hg^{2+} induced aggregation of L-Trp@GNPrs with addition of different Hg^{2+} concentrations. ($[Hg^{2+}]$ = 2 nM (a); 4 nM (b); 5 nM (c) and 6 nM (d), respectively).

19 LOD calculation by plotting ΔF vs. [Hg(II)]

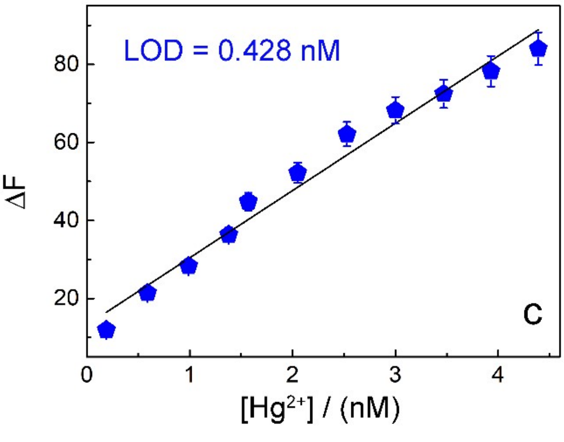

Figure S19. Determination of LOD by plotting ΔF against $[Hg^{2+}]$ and was found to be 0.428 nM.

Table S4. Tabulated form of the comparison of different optical nanoprobes for detection of Hg^{2+} ions with different spectroscopic techniques.

Method	Probe	Reagent	Detection of metal ions	LoD (nM)	Refference
Fluorescence Specrophotometry	Au@Ag	dipeptide β-Ala-Trp (β-Ala is β-alanine; Trp is L-tryptophan)	Hg(II)	9	31
	RB-AuNP	Thiol ligands (MPA, MSA, HCys) and chelating ligand (PDCA)	Hg(II)	10	32
	QDC	Dual-emitting quantum dot	Hg(II)	85.5	33
	C-NP	C-NP and rhodamine B dye hybride	Hg(II)	45	34
	AuNPs	Vancomycin functionalized gold nanoparticles	Hg(II)	0.98	35
SERS	AuNPs	Tryptophan	Hg(II)	24.9	36
Fluorimetry & SERS	L-Trp@GNPrs	L-Trptophan	Hg(II)	0.43 & 3.3	Present study

20. Effect of EDTA on the Electron Microscopy of L-Trp@GNPrs-Hg adducts

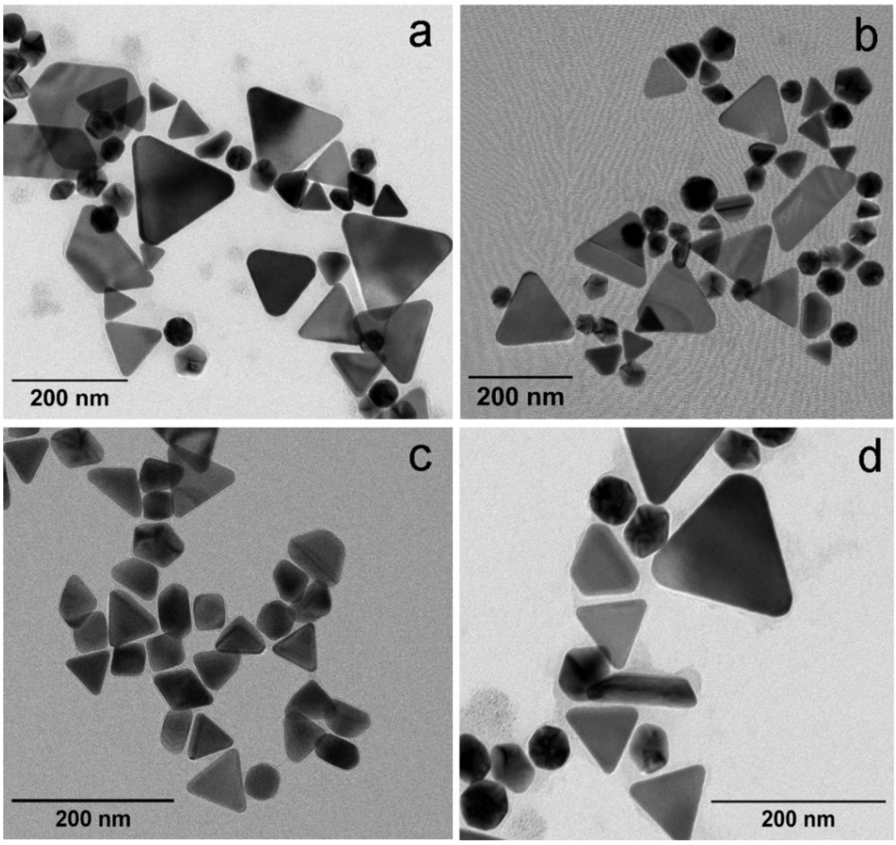

Figure S20. Electron imaging of L-Trp@GNPrs-Hg adducts with addition of different concentration of EDTA. ([EDTA] = 2 nM (a); 4 nM (b); 5 nM (c) and 6 nM (d), respectively).

21. SERS-based sensing of Hg (II) by using L-Trp@GNPrs

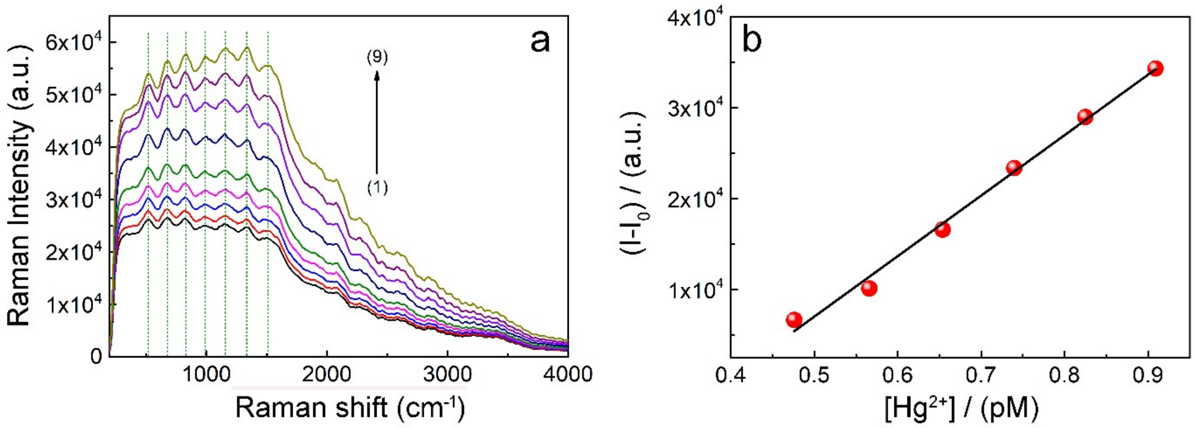

Figure S21. (a) Raman spectra of synthesized L-Trp@GNPrs in absence and presence of Hg^{2+}; curves (1-9) of (a) represent the spectral changes of L-Trp@GNPrs (47.14 μM) on addition of 0.0, 0.09, 0.30, 0.47, 0.56, 0.65, 0.74, 0.82, and 0.90 pM of Hg^{2+} and (b) LOD value was determined by plotting $(I\text{-}I_0)$ at 1338 cm^{-1} against $[Hg^{2+}]$ and was found to be 3.3 pM.

Table S5. Observed Raman stretching bands of an aqueous solution of L-Trp@GNPrs.

Observed frequency (cm^{-1})	Band Assignment
600–640	low-frequency ring deformation / skeletal C–C vibrations (often out-of-plane modes)
740–780	ring-breathing / out-of-plane aromatic deformation (common in indole / aromatic residues)
860–920	C–C / C–N single-bond stretches or wagging modes (fingerprint region)
980–1020	symmetric ring/C–C stretching or skeletal breathing (strong, sharp band in many organics)
1100–1150	C–N / C–C stretching; C–O stretches depending on chemistry
1230–1280	amide III / CH2 twisting or C–N stretching (protein/peptide fingerprint)
1350–1400	CH bending/ring breathing overtones
1580–1650	aromatic C=C stretching / amide I (if protein/peptide present)
2800–3050	C–H stretching region (aliphatic and aromatic C–H stretches)

Table S6. Antibacterial potency of both L-Trp@GNPrs and control.

Sample	Microorganisms	Zone Diameter (cm) Conc. (50µg/ml)	Zone Diameter (cm) Conc. (100 µg/ml)	Zone Diameter (cm) Conc. (200 µg/ml)
L-Trp@GNPrs	*S. aureus* ATCC 29737	1.7 ± 0.18	2.3 ± 0.26	2.8 ± 0.13
	E. coli MTCC 40	1.8 ± 0.08	2.5 ± 0.61	2.9 ± 0.37
Control (L-Trp)	*S. aureus* ATCC 29737	Nil	Nil	Nil
	E. coli MTCC 40	Nil	Nil	Nil

References

1 A. B. Pradhan, L. Haque, S. Bhuiya and S. Das, Exploring the mode of binding of the bioflavonoid kaempferol with B and protonated forms of DNA using spectroscopic and molecular docking studies, *RSC Adv.,* 2015, **5** (14), 10219–10230.

2 S. Das, S. Pramanik, S. Chatterjee, P. P. Das, P. S. Devi and G. Suresh Kumar, Selective binding of genomic Escherichia coli DNA with ZnO leads to white light emission: a new aspect of nano–bio interaction and interface, *ACS Appl. Mater. Interfaces,* 2017, **9** (1), 644–657.

3 A. Mishra, M. K. Ekka and S. Maiti, Influence of ionic liquids on thermodynamics of small molecule–DNA interaction: The binding of ethidium bromide to calf thymus DNA, *J. Phys. Chem. B*, 2016, **120** (10), 2691–2700.

4 N. C. Garbett, N. B. Hammond and D. E. Graves, Influence of the amino substituents in the interaction of ethidium bromide with DNA, *Biophys. J.,* 2004, **87** (6), 3974–3981.

5 F. A. Tanious, J. M. Veal, H. Buczak, L. S. Ratmeyer and W. D. Wilson, DAPI (4', 6-diamidino-2-phenylindole) binds differently to DNA and RNA: minor-groove binding at AT sites and intercalation at AU sites, *Biochemistry,* 1992, **31** (12), 3103–3112.

6 M. J. Frisch, G.W. Trucks, H. B. Schlegel, G. E. Scuseria, M. A. Robb, J. R. Cheeseman, G. Scalmani, V. Barone, B. Mennucci, G. A. Petersson, H. Nakatsuji, M. Caricato, X. Li, H. P. Hratchian, A. F. Izmaylov, J. Bloino, G. Zheng, J. L. Sonnenberg, M. Hada, M. Ehara, K. Toyota, R. Fukuda, J. Hasegawa, M. Ishida, T. Nakajima, Y. Honda, O. Kitao, H. Nakai, T. Vreven, J. A. Montgomery, Jr. J. E. Peralta, F. Ogliaro, M. Bearpark, J. J. Heyd, E. Brothers, K. N. Kudin, V. N. Staroverov, T. Keith, R. Kobayashi, J. Normand, K. Raghavachari, A. Rendell, J. C. Burant, S. S. Iyengar, J. Tomasi, M. Cossi, N. Rega, J. M. Millam, M. Klene, J. E. Knox, J. B. Cross, V. Bakken, C. Adamo, J. Jaramillo, R. Gomperts, R. E. Stratmann, O. Yazyev, A. J. Austin, R. Cammi, C. Pomelli, J. W. Ochterski, R. L. Martin, K. Morokuma, V. G. Zakrzewski, G. A. Voth, P. Salvador, J. J. Dannenberg, S. Dapprich, A. D. Daniels, O. Farkas, J. B. Foresman, J. V. Ortiz, J. Cioslowski and D. J. Fox, Gaussian, Inc., Gaussian 09, Revision D.01, Wallingford CT, 2013.

7 A. D. Becke, Density-functional thermochemistry. I. The effect of the exchange-only gradient correction, *J. Chem. Phys.,* 1993, **98**, 5648–5652.

8 W. J. Hehre, R. Ditchfield and J. A. Pople, Self-consistent molecular orbital methods. XII. Further extensions of Gaussian-type basis sets for use in molecular orbital studies of organic molecules, *J. Chem. Phys.,* 1972, **56**, 2257–2261.

9 P. J. Hay and W. R. Wadt, Ab initio effective core potentials for molecular calculations. Potentials for the transition metal atoms Sc to Hg, *J. Chem. Phys.,* 1985, **82** (1), 270–283.

10 W. J. Hehre, R. Ditchfield and J. A. Pople, Self—consistent molecular orbital methods. XII. Further extensions of Gaussian—type basis sets for use in molecular orbital studies of organic molecules, *J. Chem. Phys.,* 1972, **56** (5), 2257–2261.

11 M. M. Francl, W. J. Pietro, W. J. Hehre, J. S. Binkley, M. S. Gordon, D. J. DeFrees and J. A. Pople, Self-consistent molecular orbital methods. XXIII. A polarization-type basis set for second-row elements, *J. Chem. Phys.,* 1982, **77** (7), 3654–3665.

12 T. Lu and F. Chen, Multiwfn: A multifunctional wavefunction analyzer, *J. Comput. Chem.,* 2012, **33** (5), 580–592.

13 H. M. Berman, J. Westbrook, Z. Feng, G. Gilliland, T. N. Bhat, H. Weissig, I. N. Shindyalov and P. E. Bourne, The protein data bank, *Nucleic Acids Res*., 2000, **28** (1), 235–242.

14 G. M. Morris, R. Huey, W. Lindstrom, M. F. Sanner, R. K. Belew, D. S. Goodsell and A. J. Olson, AutoDock4 and AutoDockTools4: Automated docking with selective receptor flexibility, *J. Comput. Chem.,* 2009, **30** (16), 2785–2791.

15 Dassault Systemes. BIOVIA, BIOVIA Discovery Studio, Version 2020, Dassault Systèmes: San Diego, 2020.

16 A. Ghosh, S. Das, D. Senapati and U. K. Sur, Colorimetric sensing of metal ions using biosynthesized silver nanoparticles, *Interactions*, 2024, 245 (1), 190.

17 Y. Zhang, L. Zhang, L. Wang, G. Wang, M. Komiyama and X. Liang, Colorimetric determination of mercury (II) ion based on DNA-assisted amalgamation: a comparison study on gold, silver and Ag@ Au Nanoplates, *Microchim. Acta*, 2019, 186 (11), 713.

18 S. F. Mertens, M. Gara, A. S. Sologubenko, J. Mayer, S. Szidat, K.W. Krämer, T. Jacob, D. J. Schiffrin and T. Wandlowski, Au@ Hg nanoalloy formation through direct amalgamation: structural, spectroscopic, and computational evidence for slow nanoscale diffusion, *Adv. Funct. Mater.* 2011, 21 (17), 3259–3267.

19 I. Saha, S. Ghosh, A. Mondal, S. Roy, T. Basu, A. Sengupta, D. Das and P. Karmakar, Fabrication and Therapeutic Process of a Green Silver-Nanoparticle-Embedded Mucilage Microsphere for Pathogenic-Bacteria-Infected Second-Degree Burn and Excision Wounds, *ACS Appl. Bio Mater.,* 2024, **7** (4), 2554–2568.

20 S. Das, A. De, B. Das, B. Mukherjee and A. Samanta, Development of gum odina-gelatin based antimicrobial loaded biodegradable spongy scaffold: A promising wound care tool, *J. Appl. Polym. Sci.,* 2021, **138** (12), 50057.

21 A. Ghosh, S. Kumar De, S. Mondal, A. Halder, M. Barai, K. Chandra Guchhait, P. Raul, S. Karmakar, C. Ghosh, A. Patra, A. Kumar Panda, D. Senapati and U. K. Sur, Green Synthesis of Silver Nanoparticles and Its Applications as Sensor, Catalyst, and Antibacterial Agent, *Materials Today: Proceedings,* 2023.

22 M. Hosny, A. S. Eltaweil, M. Mostafa, Y. A. El-Badry, E. E. Hussein, A. M. Omer and M. Fawzy, Facile synthesis of gold nanoparticles for anticancer, antioxidant applications, and photocatalytic degradation of toxic organic pollutants, *ACS Omega,* 2022, **7** (3), 3121–3133.

23 S. Chatterjee, A. Mohanta, A. De, A. Mukherjee, A. Hazra, P. P. Niloy, M. Tudu, K. Chattopadhyay and A. Samanta, Evaluation of gum odina/carbopol composite mucoadhesive hydrogel on pharmaceutical performance: Focusing on potential periodontal treatment, *Int. J. Biol. Macromol.,* 2025, **288**, 138708.

24 K. Rurack and M. Spieles, Fluorescence quantum yields of a series of red and near-infrared dyes emitting at 600−1000 nm, *Anal. Chem.,* 2011, **83** (4), 1232–1242.

25 P. Basu, D. Bhowmik and G. S. Kumar, The benzophenanthridine alkaloid chelerythrine binds to DNA by intercalation: Photophysical aspects and thermodynamic results of iminium versus alkanolamine interaction, *J. Photochem. Photobiol. B Biol.*, 2013, **129**, 57–68.

26 L. Haque, A. B. Pradhan, S. Bhuiya and S. Das, Exploring the comparative binding aspects of benzophenanthridine plant alkaloid chelerythrine with RNA triple and double helices: a spectroscopic and calorimetric approach, Phys. Chem. Chem. Phys., 2015, **17** (26), 17202–17213.

27 M. M. Islam, R. Sinha and G. S. Kumar, RNA binding small molecules: studies on t-RNA binding by cytotoxic plant alkaloids berberine, palmatine and the comparison to ethidium, *Biophys. Chem.*, 2007, **125** (2-3), 508–520.

28 A. Sischka, K. Toensing, R. Eckel, S. D. Wilking, N. Sewald, R. Rios and D. Anselmetti, Molecular mechanisms and kinetics between DNA and DNA binding ligands, Biophys. J., 2005, **88** (1), 404–411.

29 H. Fritzsche, H. Triebel, J. B. Chaires, N. Dattagupta and D. M. Crothers, Studies on the interaction of anthracycline antibiotics and deoxyribonucleic acid: geometry of intercalation of iremycin and daunomycin, Biochem., 1982, **21** (17), 3940–3946.

30 A. H. Hu, Q. X. Duan, X. Y. Xiong, Z. Kang, A. M. Bai, M. M. Yin and Y. J. Hu, Revealing the effects of ligands of silver nanoclusters on the interactions between them and ctDNA: Abstraction to visualization, *Int. J. Biol. Macromol.*, 2023, **236**, 123965.

31 S. Guha, S. Roy and A. Banerjee, Fluorescent Au@Ag core–shell nanoparticles with controlled shell thickness and Hg (II) sensing, *Langmuir*, 2011, **27** (21), 13198−13205.

32 C. C. Huang and H. T. Chang, Selective gold-nanoparticle-based "turn-on" fluorescent sensors for detection of mercury (II) in aqueous solution, *Anal. Chem.* 2006, **78** (24), 8332−8338.

33 M. Manna, S. Roy, S. Bhandari and A. Chattopadhyay, A dual-emitting quantum dot complex nanoprobe for ratiometric and visual detection of Hg^{2+} and Cu^{2+} ions, *J. Mater. Chem. C*, 2020, **8** (21), 6972−6976.

34 M. Lan, J. Zhang, Y.-S. Chui, P. Wang, X. Chen, C.-S. Lee, H.-L. Kwong and W. Zhang, ACS Appl. Mater. & Interfaces, 2014, **6**, 21270.

35 A. K. Tiwari, H. P. Yadav, M. K. Gupta, R. J. Narayan and P. C. Pandey, Synthesis of vancomycin functionalized fluorescent gold nanoparticles and selective sensing of mercury (II), *Front. Chem.* 2023, **11**, 1238631.

36 T. Senapati, D. Senapati, A. K. Singh, Z. Fan, R. Kanchanapally and P. C. Ray, Highly selective SERS probe for Hg (II) detection using tryptophan-protected popcorn shaped gold nanoparticles. *Chem. Comm.*, 2011. **47** (37), 10326−10328.